The Astrophysical Journal, 692:1110–1124, 2009 February 20 doi:10.1088/0004-637X/692/2/1110

OBSERVATIONAL ANALYSIS OF MAGNETIC RECONNECTION SEQUENCE

Jiong Qiu
Physics Department, Montana State University, Bozeman, MT 59717-3840, USA; qiu@physics.montana.edu
Received 2008 July 17; accepted 2008 October 27; published 2009 February 23

ABSTRACT

We conduct comprehensive analysis of an X2.0 flare to derive quantities indicative of magnetic reconnection in solar corona by following temporally and spatially resolved flare ribbon evolution in the lower atmosphere. The analysis reveals a macroscopically distinctive two-stage reconnection marked by a clear division in the morphological evolution, reconnection rate, and energy release rate. During the first stage, the flare brightening starts at and primarily spreads along the polarity inversion line (PIL) with the maximum apparent speed comparable to the local Alfvén speed. The second stage is dominated by ribbon expansion perpendicular to the PIL at a fraction of the local Alfvén speed. We further develop a data analysis approach, namely *reconnection sequence analysis*, to determine the connectivity and reconnection flux during the flare between a dozen magnetic sources defined from partitioning the photospheric magnetogram. It is found that magnetic reconnection proceeds sequentially between magnetic cells, and the observationally measured reconnection flux in major cells compare favorably with computations by a topological model of magnetic reconnection. The three-dimensional evolution of magnetic reconnection is discussed with respect to its implication on helicity transfer and energy release through reconnection.

Key words: Sun: activity – Sun: flares – Sun: magnetic fields

Online-only material: color figure

1. INTRODUCTION

Magnetic reconnection governs explosive energy release on the Sun as manifested in solar flares. In the past decades, observations of flares across the entire atmosphere have given rise to the standard flare model, which is primarily a two-dimensional configuration. The model captures many macroscopic flare signatures (see review by Priest & Forbes 2000) and provides a successful qualitative explanation of the evolution and geometry of the often observed two-ribbon flares (Svestka & Cliver 1992). However, magnetic reconnection in the Sun's corona is three-dimensional by nature. The observed magnetic field on the Sun is highly structured and does not show a two-dimensional bipolar configuration as in the standard model. Even two-ribbon flares almost always exhibit complex morphologies that cannot be described by a two-dimensional picture. For example, the observed two ribbons in the positive and negative magnetic fields are often asymmetric (Fletcher & Hudson 2001), and flare brightenings are often observed to spread along the ribbon direction (Moore et al. 2001; Fletcher et al. 2004). Furthermore, lack of two-ribbon hard X-ray flares provides strong evidence that magnetic energy release is not uniform along the polarity inversion line (PIL; Sakao 1994; Krucker et al. 2005). Knowledge of the three-dimensional topological structure of the magnetic field and its change during the flare is crucial to our understanding of physics of energy storage and release as well as magnetic helicity transfer between topological structures. For the time being, such knowledge is only gained from theoretical models (see review by Demoulin 2006).

Recently, Longcope & Beveridge (2007) developed the first applicable approach to compute the change of connectivity between topological domains and subsequently the helicity transfer between magnetic structures. The model assumes an initial potential field of an active region, which gradually evolves into a nonpotential field before the major flare. This is driven by photospheric plasma motions pushing around magnetic elements, whereas the original connectivity is maintained, i.e., no reconnection or relaxation is allowed. The build-up of nonpotentiality is quantified by the helicity accumulation computed from a time sequence of photospheric magnetograms. The preflare nonpotential field can only be relaxed through magnetic reconnection during the major flare to another potential field constructed from the new boundary, the postflare magnetogram. From the difference between the two potential fields, the model can compute the amount and sequence of flux exchange between topological domains determined by photospheric magnetic elements. Importantly, these physical quantities can be tested by independent observational measurements, which provides constraints to the model thus is able to justify or falsify the calculation of helicity transfer and energy release by the model. The method was applied to an active region producing an X2.0 flare on 2004 November 7 to compute flux exchange between domains, helicity transfer, and energy release (Longcope et al. 2007).

In this paper, we present an effort toward quantitatively determining evolution of magnetic reconnection from observations. We develop an approach to analyze the connectivity between magnetic cells during magnetic reconnection, which yields the rate and sequence of magnetic reconnection to be directly compared with the model computation. Reconnection process in the corona cannot be observed directly but can be tracked via the temporal and spatial evolution of flare patches in the magnetic fields in the lower atmosphere, as has been practised by a few groups (Poletto & Kopp 1986; Fletcher & Hudson 2001; Fletcher et al. 2004; Isobe et al. 2002, 2005; Qiu et al. 2002, 2004; Saba et al. 2006). In short, following the principle of magnetic flux conservation from the corona to the lower atmosphere and on typical time and spatial scales of present observations, the coronal magnetic reconnection rate, or reconnection flux per unit time, can be measured by $\dot{\Phi} = \partial\Phi/\partial t = \partial(\int B_l dA_l)/\partial t$ (Forbes & Priest 1984). The term on the left denotes the coronal magnetic reconnection rate, or reconnection flux per unit time. On the right-hand side, B_l is the normal component of magnetic field at the locations of flare patches in the lower atmosphere,

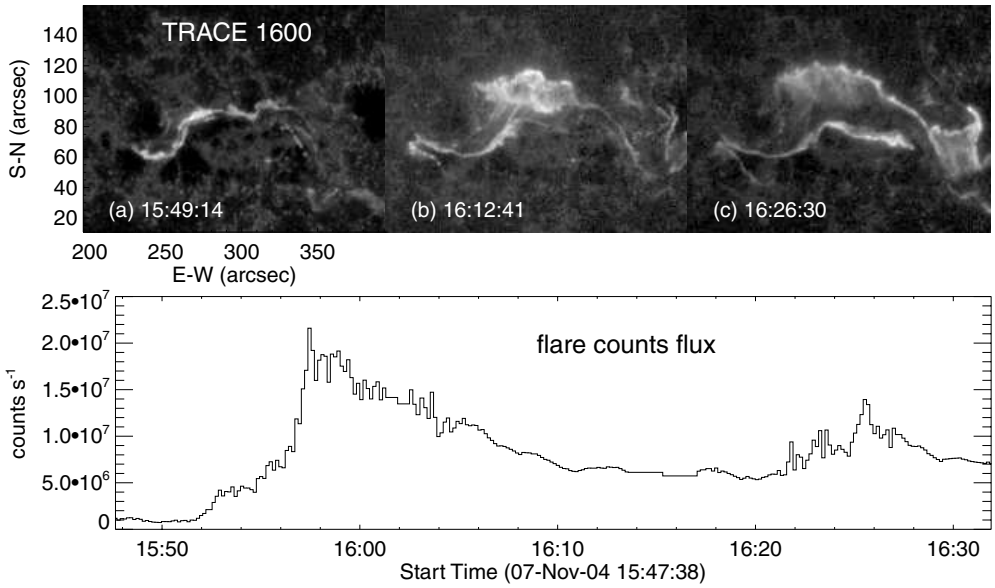

Figure 1. Top: snapshots of the X2.0 flare observed by TRACE 1600 Å on 2004 November 7. Bottom: the light curve of the count rates of the flare at 1600 Å (same as Figure 7 in Longcope et al. 2007).

which are believed to map the footpoints of field lines reconnecting in the corona, and dA_l is the elementary newly brightened flare area at the feet. In this study, we will employ this method to measure the temporally and spatially resolved reconnection rate in terms of $\dot{\Phi}$ (in units of Mx s^{-1}) and derive the sequence of magnetic reconnection between magnetic sources. In Section 2, we review the X2.0 flare previously modeled by Longcope et al. (2007). In Section 3, we quantitatively examine evolution of flare ribbons with respect to the PIL to gain observational insight into the three-dimensional evolution of magnetic reconnection. In Section 4, we describe the procedure to derive reconnection sequence and application to the flare. In Section 5, the analysis results are briefly compared with the model and discussed regarding helicity transfer and energy release. Conclusions of the paper are given in Section 6.

2. TEMPORAL AND SPATIAL EVOLUTION

The standard two-dimensional model assumes a symmetric bipolar configuration and a uniform magnetic reconnection rate along an infinitely long neutral line in the corona. However, observations reveal that the morphologies of magnetic fields and flares are asymmetric and highly structured. The complex magnetic field and flare evolution require a full three-dimensional description which deals with both the temporal and spatial evolution of magnetic reconnection. To spatially resolve magnetic reconnection, in this study, to the first-order approximation, the observed photospheric magnetic field is partitioned into individual magnetic cells based on the morphology and evolution of the active region (Barnes et al. 2005). Connectivities between these magnetic cells determine the topological structure, which is often used to describe the magnetic field in the active region (Demoulin et al. 1992, 1994; Longcope 1996).[1] Tracking the reconnection rate, inferred from flare evolution, in each of the individual magnetic cells thus provides the means to determine the sequence of magnetic reconnection between magnetic domains defined by these source elements. In the following text, we refer such analysis as *reconnection sequence analysis*.

We apply the analysis to a two-ribbon flare occurred at 16 UT on 2004 November 7 in NOAA-10696, when the active region was at the disk center. The active region was observed by Michelson Doppler Imager (MDI; Scherrer et al. 1995). The flare was observed throughout its evolution by Transition Region and Coronal Explorer (TRACE; Handy et al. 1999) in 1600 Å ultraviolet (UV) continuum with the best cadence (2 s) of the instrument and a pixel scale of 0.″5. Observations at this wavelength reflect the flare emission in the lower atmosphere, or emission at the feet of flaring loops. Longcope et al. (2007) comprehensively studied the evolution and topology of this active region and used a topological model to compute energy and helicity build-up before the explosion as well as helicity transfer and energy release during the flare. In the present study, flare observations by TRACE and magnetic field observations by MDI are employed to analyze signatures of magnetic reconnection and its three-dimensional evolution. In Figure 1, we reproduce the snapshots of the flare and the UV count rates light curve (same as Figure 7 in Longcope et al. 2007). The flare is composed of two events 40 minutes apart. The first event occurred at 15:40 UT and decayed by 16:15 UT. It took place in the core active region. The second event set off at 16:25 UT, and resided in the west of the core region. In the present study, we limit the analysis to the first event. The analysis focuses on quantitative determination of the temporal and spatial evolution of magnetic reconnection, which is a crucial step toward understanding the role of magnetic reconnection in energy release and helicity transfer.

Figure 2 (top panel) shows the longitudinal magnetogram of the active region obtained by MDI before the flare onset, which is partitioned into a set of positive (denoted by letter "P") and negative (denoted by the letter "N") magnetic cells. We adopt the same partitioning by Longcope et al. (2007), which is applied to the last magnetogram at the start of the flare. The magnetic flux in each cell is held constant during the flare with the assumption that the timescale of magnetic field evolution

[1] A thorough investigation on the effects of different ways of partitioning and extrapolation on the field topology is given by Longcope et al. (2009). These are not discussed in the present paper, which is focused on the observational analysis of reconnection.

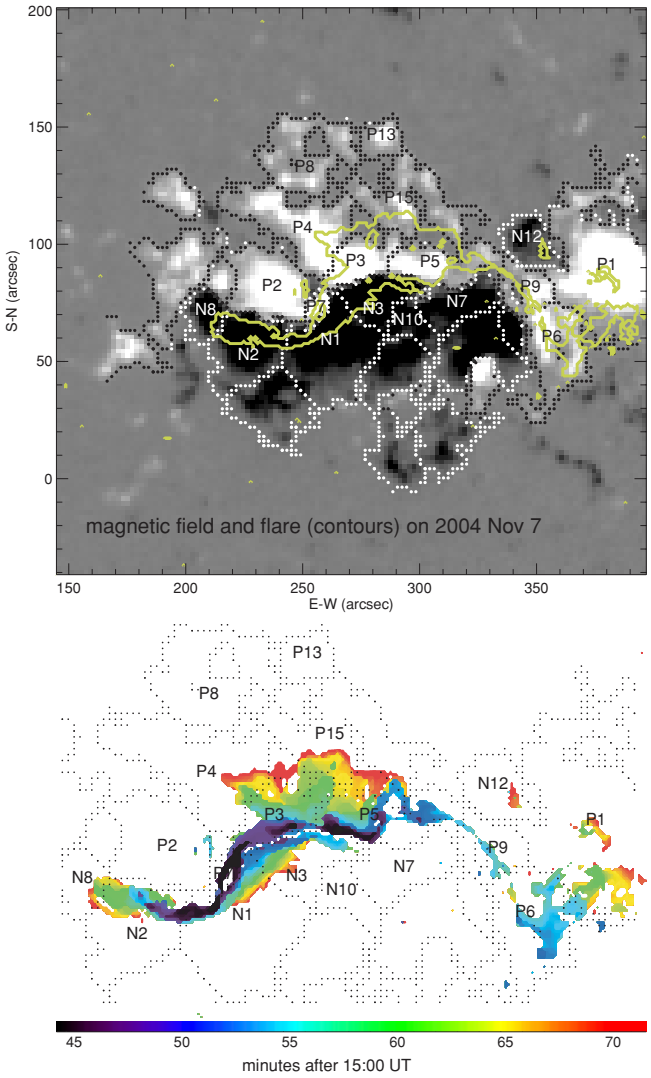

Figure 2. Top: photospheric magnetogram by MDI superimposed with the contours of flare areas at the maximum of the flare. "P" and "N" denote the positive and negative magnetic cells, respectively. Bottom: the temporal and spatial evolution of the flare superimposed on partitioned magnetogram. Time is indicated by the color code. Specifically, the number below the color bar indicates that at the time (minutes after 15:00 UT) indicated by the number, the flare ribbons expand to the areas shaded in the color above this number. For example, at 55 minutes after 15:00 UT, the flare ribbons expand to the areas shaded in light blue.

(A color version of this figure is available in the online journal.)

is much longer than the flare duration. Figure 2 (bottom panel) shows the time sequence, as indicated by the color code, of flare brightening observed at 1600 Å superimposed on the co-aligned longitudinal magnetogram. The flare exhibits the well known pattern of expanding two bright ribbons, but the magnetic fields the ribbons reside in are a lot more complex than a two-dimensional symmetric configuration.

Integrating magnetic flux in flaring regions, we derive time profiles of the total reconnection flux $\Phi(t)$ in the positive and negative polarities, as shown in Figure 3. Note that to derive the magnetic flux we use photospheric magnetograms which are multiplied by a calibration factor of 1.56 and with projection effects corrected (Longcope et al. 2007). Different calibrations may result in changes in the measured reconnection flux, but would not affect the time profiles significantly within the uncertainties of the measurements (Qiu et al. 2007). In this study, the time sequence analysis employs 30 s averaged time profiles of reconnection rates, which significantly reduces fluctuations caused by noise in the magnetograms and by uncertainties in the analysis method (see Qiu et al. 2007). It is shown that reconnection flux evolves nearly simultaneously in both polarities. Theoretically, equal amounts of positive and negative fluxes should participate in reconnection. We find that the median value of the ratio between the total reconnection fluxes measured in the positive and negative polarities is 1.1, indicating a good balance between the positive and negative fluxes, given that uncertainties in the flux measurements are in the range of 10%–20% when no magnetic field extrapolation is performed (Qiu et al. 2007). The reconnection rate $\dot{\Phi}(t)$ in units of Mx s^{-1} is computed as the time derivative of reconnection flux. On timescales of the order of 1 minute, reconnection rates $\dot{\Phi}(t)$ derived in the positive and negative polarities are correlated: they rise, peak, and decay simultaneously.

Figure 3 shows that magnetic reconnection proceeds in a few episodes. Recognizing major peaks or groups of peaks in the reconnection rate time profiles, we divide the progress of reconnection into five episodes as indicated by vertical bars in the figure. These five episodes are also grouped into two major stages with an apparent division at 54 minutes after 15:00 UT.[2] The first stage proceeds for about 10 minutes This stage involves about one-third of the total reconnection flux in both polarities. The second stage sets off with a pronouncedly increased reconnection rate, and then reconnection slows down after 63 minutes. The nominal energy release rate, as indicated by the time derivative of *GOES* soft X-ray (1–8 Å) light curve (the so-called "Neupert effect"; Neupert 1968), also exhibits a few peaks, with significant energy release taking place during the second stage. An estimate of the thermal energy release rate using *GOES* observations and geometric information of the flare will be given in the last section.

We then derive time profiles of the reconnection rate in magnetic cells determined from partitioning in Figure 2. A total of eight positive cells and six negative cells participate in the reconnection at different times during the flare. Reconnection at two different stages takes place between different pairs of magnetic cells. The first stage involves cells right next to the PIL. During this stage, individual flare kernels at a few places are brightened and then developed into two flare ribbons nearly along the PIL. Note that in this event no filament was observed in the active region, and the brightenings in the two ribbons started from the PIL with little separation between the two ribbons at the beginning. During the second stage, most cells are getting involved, and the two flare ribbons exhibit the well-known pattern of moving apart and nearly perpendicular to the PIL. This main stage of great expansion resembles the two-dimensional arcade-like reconnection (e.g., Moore et al. 2001), and is characterized by evident enhancement in the reconnection rate and greater amount of reconnection flux as well as energy release. Eventually, reconnection ends in a couple of cells a distance away from the PIL.

On macroscopic scales, the first stage is characterized by the formation of the skeleton of flare ribbons along the PIL, followed by expansion of the ribbons perpendicular to the PIL during the second stage. We, therefore, term these two distinctive evolution stages as stages of "parallel elongation" and "perpendicular expansion," respectively. In the following

[2] Hereafter, we will record time in terms of minutes after 15:00 UT in both text and figures.

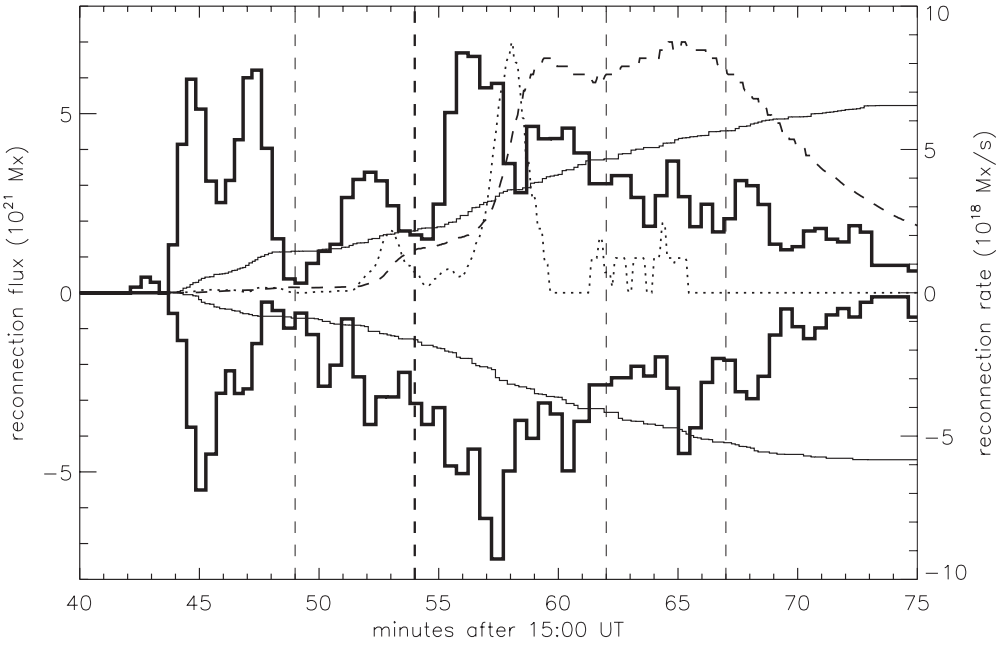

Figure 3. Time profiles of the total reconnection flux in units of Mx (thin solid line) and the reconnection rate in units of Mx s^{-1} (thick solid line) integrated in the positive and negative polarities, respectively. Also shown are soft X-ray flux at 1–8 Å observed by *GOES* (thin dashed line) and its time derivative (thin dotted line), both normalized to arbitrary units. The maximum of the *GOES* X-ray flux at 1–8 Å is 6.6×10^{-5} W m^{-2}. The vertical dashed bars indicate five episodes of magnetic reconnection: 44–49, 49–54, 54–62, 62–67, and 67–75 minutes after 15:00 UT. The thick dashed vertical bar at 54 minutes indicates the division of two major stages.

sections, we will first quantify the macroscopic evolution of the flare ribbons with respect to the PIL. Then, we will apply the *reconnection sequence analysis* to measure the reconnection sequence between individual magnetic cells, which can be communicable with theoretic or model studies.

3. ELONGATION AND EXPANSION OF FLARE RIBBONS

The distinctive two-stage evolution of flare ribbons with respect to the PIL has been reported ever since quality observations of the lower atmosphere of the flare became available. Moore et al. (2001) reported six flares exhibiting similar two-stage patterns and put forward the scenario of "tether-cutting" or "internal reconnection" followed by the "arcade reconnection" (Moore & La Bonte 1980). Kitahara & Kurokawa (1990) reported, from Hα observations, "the progressive brightenings of flare points forming the front lines of the Hα two ribbons," "followed by the explosive expansion of Hα two ribbons." The authors noted that the apparent speed of the "progressive brightenings" is on the order of 100–300 km s^{-1} (also see Kawaguchi et al. 1982), and cited Vorpahl (1972) suggestion that the sequential reconnection is triggered by a magnetosonic wave.

In this section, we devise an approach to quantitatively characterize evolution of the flare ribbons with respect to the PIL. For this purpose, we first determine the profile of the PIL from the magnetogram, which is curved and extended nearly in the east–west direction. We then decompose the spread of ribbon brightening into two directions, parallel (elongation) and perpendicular (expansion) to the local PIL. To quantify the elongation and expansion of flare ribbons, we measure the following quantities for each ribbon (see Section 3.1), or each resolved section of the ribbon (Section 3.2), at each time frame: the entire ribbon length ($l_{||}$) projected along the PIL, the distances ($d^h_{||}$ and $d^t_{||}$) of the two end points, or "head" and "tail," of the ribbon along the PIL relative to a fixed point at the eastern end of the PIL, and the mean distance ($d_\perp$) of the ribbon front perpendicular to the local PIL. The mean perpendicular distance $d_\perp$ is computed as $d_\perp = S/l_{||}$, where S is the total area enclosed between the outer edge of the ribbon and the section of the PIL along the ribbon. The time profile of $l_{||}$ gives a general description of the ribbon growth along the PIL. Time profiles of $d^h_{||}$ and $d^t_{||}$ would indicate the pattern of the apparent spread of ribbon fronts along the PIL. In this study, the "head" and "tail" refer to the brightening at the western and eastern ends of the ribbon, respectively, relative to a fixed point at the eastern end of the PIL. Therefore, a growing $d^h_{||}$ would indicate ribbon elongation westward along the PIL, and a decreasing $d^t_{||}$ would indicate ribbon elongation eastward along the PIL. On the other hand, a decrease in $d^h_{||}$ or an increase in $d^t_{||}$ would indicate "shrinkage," such as by cooling, of the ribbon along the PIL. Our analysis shows that the "shrinkage" of the flare ribbon is insignificant, suggesting that the timescale of cooling to the pre-flare radiation level is significantly longer than the timescales of reconnection evolution and heating of the lower atmosphere. The time profile of $d_\perp$ reflects expansion, if $d_\perp$ grows, of the ribbon away from the PIL.

To have a sense of uncertainties in the measurements of these quantities, we analyze flare images and magnetograms with varying thresholds of flare emissions and different temporal and spatial smoothing factors to find the mean values as well as deviations. It is found that deviations in measuring $l_{||}$, $d^h_{||}$, and $d^t_{||}$ are of order 10% of the mean values. The standard deviation of $d_\perp$ measurement at each time, as estimated by measuring $d_\perp$ in different parts of the ribbon front, ranges from 5% to 35% of the mean value for P-ribbon and from 10% to 45% of the mean value for N-ribbon. In absolute values, the maximum standard deviation is about 3.2 Mm at 54 minutes for P-ribbon, and 1.8 Mm at 52 minutes for N-ribbon. The mean standard deviation is 0.7 Mm for P-ribbon and 0.9 Mm for N-ribbon, respectively. These numbers refer to measurements before 70 minutes. After 70 minutes, the number of pixels of the ribbon front is too small for meaningful estimates. For the same reason,

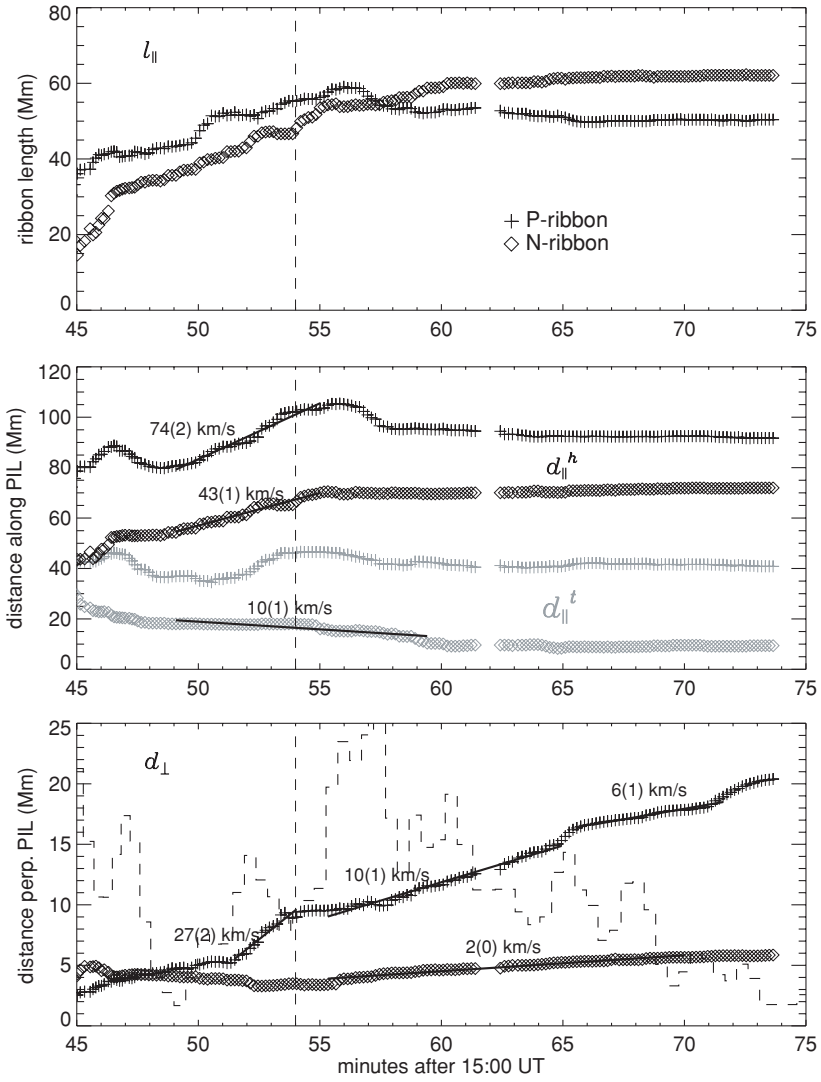

Figure 4. Global evolution of flare ribbons with respect to the PIL. Top: the total length $l_{||}$ of flare ribbons along the PIL. Middle: the distances of the "head" ($d_{||}^{h}$, dark symbols) and "tail" ($d_{||}^{t}$, gray symbols) points of the ribbon front along the PIL. Bottom: the mean distance $d_{\perp}$ of the ribbon front perpendicular to the PIL. In all panels, the vertical dashed bar at 54 minutes indicates the division between two major stages of reconnection. In the bottom panel, the dashed curve indicates the total reconnection rate (the mean of the total reconnection rates derived from the positive and negative polarities) arbitrarily normalized. The mean apparent speeds of flare ribbon elongation or expansion at different times are marked in the figures, and the numbers in the parentheses denote the σ in the speed derived from the least-squared fit.

we do not compute the standard deviation in $d_{\perp}$ measurements within individual cells but adopt the deviations computed from different analysis runs with varying thresholds, which are of order 10%.

In the following text, we first derive the general pattern of ribbon evolution in terms of these quantities, and then analyze the spatially resolved pattern, particularly during the early stage of the flare, by measuring the evolution within individual magnetic cells.

3.1. General Evolution Pattern

Figure 4 shows the time evolution of $l_{||}$ (top panel), $d_{||}^{h}$ and $d_{||}^{t}$ (middle panel), and $d_{\perp}$ (bottom panel) for the two ribbons in the positive (P-ribbon hereafter) and negative (N-ribbon hereafter) polarities. The flare evolution in two stages, divided at around 54 minutes, is evident in these plots.

The top panel shows that the gross length of each ribbon along the PIL grows from the start of the flare to about 54 minutes, when both ribbons have extended along the PIL for 50–60 Mm. Note that $l_{||}$ measures the instantaneous maximum extension of the entire ribbon, other than the newly brightened front of the ribbon, along the PIL, which stops growing after 54 minutes. In the middle panel, we find apparent westward elongation of the ribbon in both ribbons up to 54 minutes, and apparent eastward elongation is also evident in the N-ribbon until 59 minutes. In other words, the apparent elongation is primarily unidirectional in P-ribbon and bidirectional in N-ribbon during the first stage. The bottom panel shows that the mean perpendicular distance of the ribbon front from the PIL starts to grow from 52 minutes in P-ribbon and from 54 minutes in N-ribbon, and the growth of $d_{\perp}$ in both ribbons continues until after 70 minutes. This reflects the ribbon spread perpendicular to the PIL, or the "expansion" motion as per our definition. In summary, the plots quantitatively illustrate the two-stage evolution of flare ribbons: dominant elongation of both ribbons along the PIL before 54 minutes and dominant expansion of both ribbons perpendicular to the PIL after 54 minutes. This is indicative of the manner of two-stage reconnection in the corona.

We estimate the mean speed of the apparent ribbon spread in the lower atmosphere by fitting time profiles of the measured quantities as linear functions of time wherever appropriate. From the top panel, the mean "growth" rate of the ribbon length up to 54 minutes amounts to 40 km s^{-1}. From the middle panel, the apparent speed of the front along the PIL is 70 km s^{-1} for the P-ribbon, and 10–40 km s^{-1} for the N-ribbon, with a faster elongation to the west than to the east. From the bottom panel, we estimate the mean speed of apparent expansion for P-ribbon to be nearly 30 km s^{-1} from 52 minutes, reducing to 6–10 km s^{-1} after 54 minutes, and 2 km s^{-1} for N-ribbon from 54 minutes onward. When following certain locations of fastest expansion along the ribbon, we measure the maximum expansion speed up to 20 km s^{-1} in the N-ribbon, while along the P-ribbon, the perpendicular expansion is nearly homogeneous at all locations. Uncertainties, or deviations of different analysis runs and the fitting procedure, are of order 10% of the measured mean speeds. The measured speeds of the apparent motions are a fraction of, and at times maybe comparable with, the local Alfvén speed, which is approximately 100–200 km s^{-1} in the lower atmosphere[3] given an average plasma density of 10^{12-14} cm^{-3} and magnetic field of 100–500 G in the active region. We also note that the flare ribbon in the positive polarity spreads, either parallel or perpendicular to the PIL, with a greater speed than in the negative polarity. This is a result of balanced magnetic reconnection flux, as the negative ribbon resides in stronger field, while the positive ribbon expands into weaker fields.

The apparent speed of ribbon elongation parallel to the PIL in the lower atmosphere manifests the rate of reconnection spreading along the assumed direction of the reconnection current sheet in the corona. The Alfvén Mach number of the apparent speed in the corona $M_c = V_c/V_{ca}$ may be estimated starting with the flux conservation $B_c A_c = B_l A_l$, where A_c is the area through which reconnecting field lines sweep in the corona in a given instant, A_l is the newly brightened area swept by the flare in the lower atmosphere, and B_c and B_l indicate magnetic field in the corona and lower atmosphere, respectively. We may approximate A_c and A_l by $A_c \approx V_c l_c \delta t$ and $A_l \approx V_l l_l \delta t$, where V, l, and δt are the instantaneous apparent speed, a characteristic length perpendicular to V, and a given time interval during which reconnection takes place. Subscripts c and l indicate the parameters in the corona and lower atmosphere, respectively. Assuming that within a given instance, δt and l are identical in the corona and the chromosphere (as long as δt is longer than timescales of energy release and transfer), we arrive at $M_c/M_l = (V_c/V_{ca})/(V_l/V_{la}) = (B_l/B_c \times \sqrt{\rho_c})/(B_c/B_l \times \sqrt{\rho_l}) = B_l^2/B_c^2 \times \sqrt{\rho_c/\rho_l}$, where ρ is the plasma density. Order-of-magnitude, given the ratio of the magnetic field in the corona to the field in the chromosphere, and the ratio of plasmas density, it is seen that $M_c/M_l \approx B_l^2/B_c^2 \times \sqrt{\rho_c/\rho_l} \geqslant 1$. With the measured $M_l \sim 0.1$–0.7, we therefore arrive at $M_c \geqslant 0.1$–0.7. This is to say, the maximum apparent speed of reconnection spreading in the corona is nearly comparable to the coronal Alfvén speed during the stage of parallel elongation, when the reconnection spreads nearly along the PIL. The measurements in this event observed at 1600 Å are smaller than the speed measured by Kitahara & Kurokawa (1990) studying observations at Hα line center, but larger than the apparent speed measured by Fletcher et al. (2004), who also studied observations in the 1600 Å UV continuum. However, for purposes different from this study, Fletcher et al. (2004) made the measurements by identifying and following individual kernels, while in our measurements we track the emitting features above a designated threshold at the two ends of the ribbon along the PIL. The measured speed of the "head" and "tail" along the ribbon yields an estimate of "spread" of reconnection along the PIL, and is not necessarily the apparent speed of a coherent kernel by Fletcher et al. (2004). Note that these parallel speeds measured in this paper and by Fletcher et al. (2004) are not chromospheric projection of the reconnection inflow speed, but may be viewed as the rate of perturbation propagation, the physical mechanism for which remains unknown, along the presumed direction of the reconnection current sheet. On the other hand, the speed of the apparent expansion perpendicular to the PIL may be interpreted as the projection of the coronal inflow speed, which makes an appreciable fraction of the Alfvén speed ($M_c \geqslant M_l \sim 0.1$ at the maximum in this event).

Our analysis reveals "unzipping" of magnetic reconnection along the PIL before the perpendicular expansion predominates. The same or similar phenomena have been reported in previous studies. Apart from the traditional Hα observations of flare ribbons (Kitahara & Kurokawa 1990; Moore et al. 2001), Su et al. (2007) showed the bright points observed by TRACE with an initial trajectory more parallel than perpendicular to the PIL. Krucker et al. (2005), Liu et al. (2006), Des Jardins (2007), and Grigis & Benz (2008) showed the parallel motion of hard X-ray footpoints along the PIL using RHESSI observations. These later observations, particularly hard X-ray observations, however, focus on localized sites of the strongest emission, presumably the sites of strongest energy release, whereas our analysis with an emphasis on reconnection sequence takes information of the entire ribbon by analyzing all the radiation enhancement produced by reconnection energy release.

3.2. Spatially Resolved Evolution

The above analysis yields the general pattern of flare ribbon evolution, by treating each of the two ribbons as a continuously extended patch. Examining the TRACE flare movie, we note that at the start of the flare, brightenings took place at a few spatially separated kernels. From 44 to 49 minutes, the spread of flare brightenings along the ribbons is less in order, and is dominated by the brightening filling up the gaps between bright kernels. The elongation pattern became organized, or directional, after 49 minutes. To study these details in the initial stage of the flare, we analyze the spatially resolved evolution by measuring $d_{||}$ and $d_{\perp}$ in each of the magnetic cells.

Figure 5 shows time profiles of $d_{||}$ and $d_{\perp}$ for six major cells, P3, P5, and P4, in the positive fields, and N1, N2, and N3, in the negative fields. Vertical bars on each curve indicate measurement uncertainties. Since the length of the ribbon front in each cell is very small, we do not compute the standard deviation of $d_{\perp}$ measurements at each time. As the primary purpose is to study spatial evolution particularly during the early stage, we do not present analysis in other cells, except P4, involved at later times. Also note that even though brightening in the cell P7 occurs at the start of the flare, the flare kernel in P7 rapidly increases in area within 2–3 minutes and does not exhibit a clear pattern of elongation or expansion. Therefore, measurements in P7 are not presented. In each plot, the elongation (in both directions) and expansion of the flare brightening are captured for each cell. These plots show that,

[3] With respect to the 1600 Å UV continuum radiation, the lower atmosphere would refer to the chromosphere and below down to the temperature minimum region.

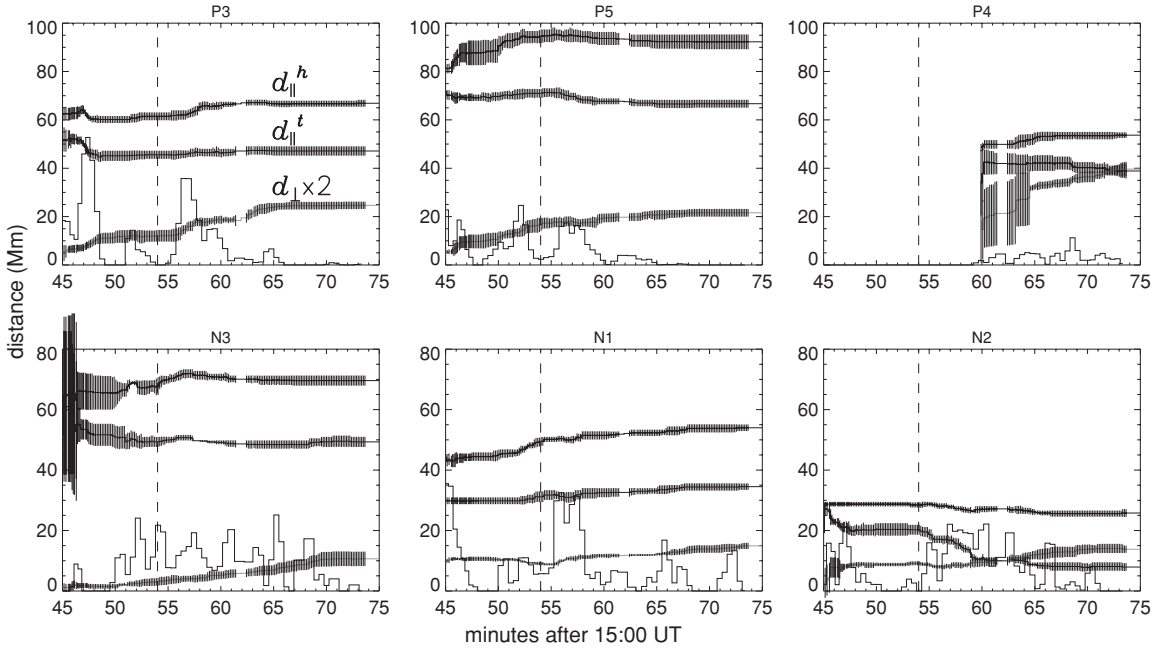

Figure 5. Spatially resolved evolution of flare brightenings in magnetic cells. In each panel, the three curves from the top to the bottom show measurements (in units of Mm) of $d_{||}^{h}$, $d_{||}^{t}$, and $d_{\perp}$, respectively, of the ribbon front in a major reconnection cell. Note that $d_{\perp}$ is magnified by a factor of 2 for clarity. The vertical bars on the curve indicate the measurement uncertainty. In each panel, the thin solid curve shows the reconnection rate in the cell in units of 10^{17} Mx s^{-1}.

though less pronounced, the two-stage reconnection is reflected in individual cells as well. In most cells, elongation along the PIL is prominent between 49 and 54 minutes, and perpendicular expansion dominates afterward.

The figure also reveals a few details during the first stage, which are not seen in the global pattern. First, at the onset, brightenings started impulsively and simultaneously (within the cadence of the observation) at a few separate sites in different cells, P3, P5, the boundary of N1 and N2, and also in the middle of N3 two minutes later. The approximate size of the kernel may be estimated from the distance between the "head" and "tail" at the first time frame. The kernel inside P5 is piece-like, of 10 Mm, or about 7 MDI pixels. Some other kernels are close to point sources (with the size comparable to the instrument resolution). Second, the figure shows a precursor episode from 44 to 49 minutes, when all individual kernels are both elongating and expanding, filling up gaps between separate kernels into a continuous piece of flare ribbon, which then elongates along both the western and eastern directions. Note that in this precursor episode when brightening starts in the UV-1600 Å continuum, no enhancement in the *GOES* X-ray emission is observed. From 49 to 54 minutes, the cell P3 exhibits an elongation motion eastward, while P5 primarily elongates westward. In the negative polarity, N3 elongates bidirectionally. N1 elongates westward and N2 elongates eastward, both from a middle point between N1 and N2. The spatially resolved analysis yields speeds of the apparent expansion comparable with the values derived for the global pattern. The apparent elongation speed within individual cells is somewhat smaller than the maximum elongation speed seen in Figure 4, because the global elongation includes brightenings successively across adjacent cells, particularly along the PIL from P5 to P9 and P6.

4. RECONNECTION SEQUENCE ANALYSIS

The quantitative approach to determine the reconnection sequence is through a correlation analysis between reconnection rates derived in individual magnetic cells determined from partitioning in Figure 2. In principle, within a given interval, energy release takes place simultaneously at conjugate footpoints of magnetic field lines that are reconnecting. Therefore, the reconnection fluxes at these sites evolve along with each other with balanced positive and negative fluxes. With this principle, we develop an approach to pick out pairs of magnetic cells that are reconnecting within a given interval.

We denote the time profile of the reconnection rate of a positive cell during a given time interval as $\dot{\Phi}_p(t, t+\Delta t)$, where p is from 1 to N_p, N_p being the number of positive cells, and denote that of a negative cell during the same interval as $\dot{\Phi}_n(t, t+\Delta t)$, where n is from 1 to N_n, N_n being the number of negative cells. Note that $\dot{\Phi}_p$ and $\dot{\Phi}_n$ are reconnection rates, or the time derivative of reconnection flux in the cells, derived from the equation in Section 1 and are not normalized to their maxima. If $\dot{\Phi}_p(t, t+\Delta t)$ and $\dot{\Phi}_n(t, t+\Delta t)$ are correlated with a significant cross-correlation coefficient (e.g., greater than 0.5), these two magnetic cells p and n are considered to be reconnecting during this interval from t to $t+\Delta t$. In practice, most magnetic cells are involved in magnetic reconnection with multiple cells at multiple times with different start and end times. If we divide the entire duration of the flare into intervals with fixed start and end times by any means and perform cross-correlation during these intervals, we would miss out a significant number of peaks that span two fixed intervals. Therefore, we devise running intervals with a fixed length of $\Delta t = 5$ minutes (10 time bins) such that the first interval starts from the time bin 1 and ends at time bin 10, the second interval starts from time bin 2 and ends at 11, and so forth, and cross-correlate $\dot{\Phi}_p(t_i, t_i+\Delta t)$ and $\dot{\Phi}_n(t_i, t_i+\Delta t)$ for any set of p and n over $i = 1, N_t - 9$, where N_t is the total number of time bins. The length of the interval should be chosen in such a way that any single reconnection peak can be covered within a certain interval, while any given interval does not include more than one reconnection peak. Noting that the typical duration of an individual reconnection

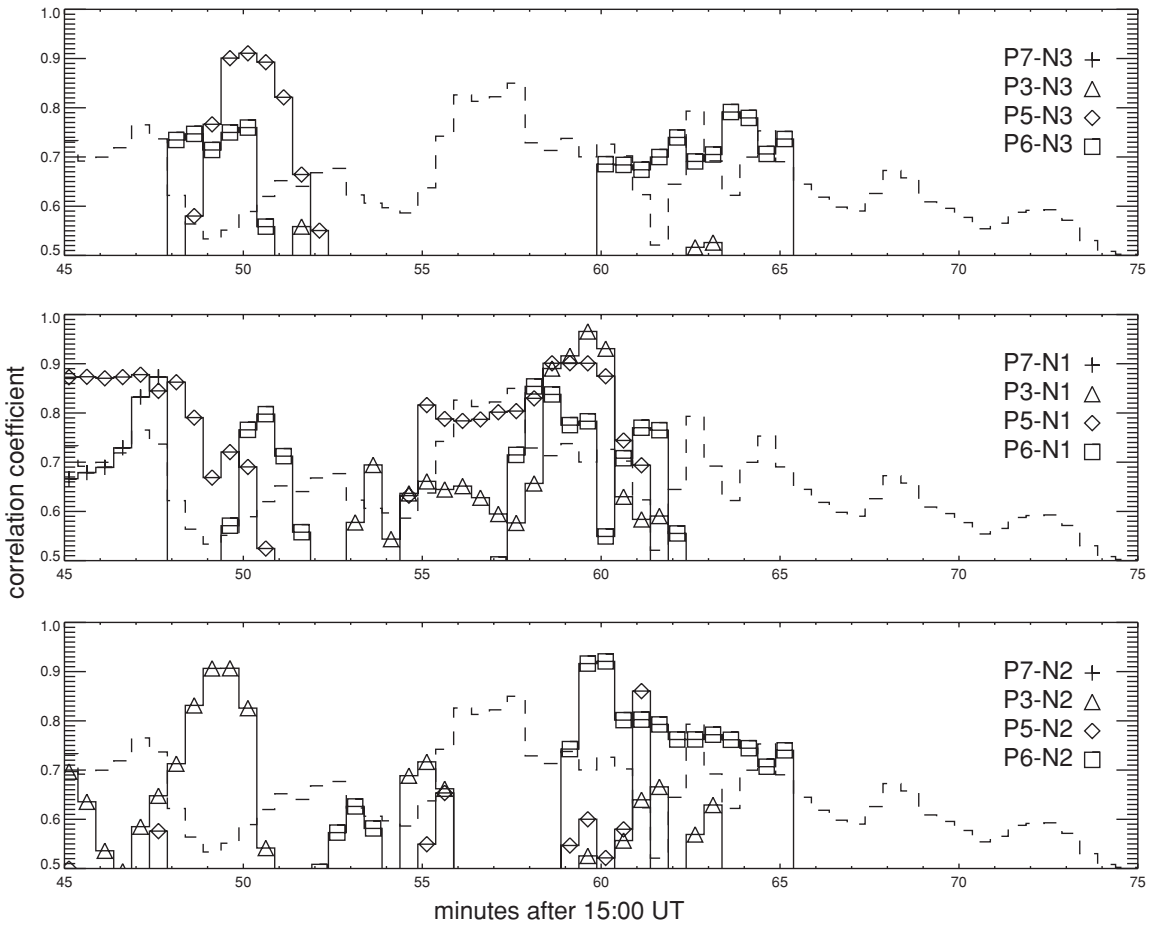

Figure 6. Time profiles of cross-correlation coefficients ρ_{pn} between the three major negative cells N3 (top panel), N2 (middle panel), and N1 (bottom panel) and eight positive cells P7, P3, P5, P6, P9, P4, P15, and P1. Symbols indicate coefficients of cross-correlation between individual magnetic cells during the 5 minute (10 bin) interval centered at the time bin. Dashed lines show the total reconnection rate arbitrarily normalized.

peak is $\leqslant$ 5 minutes, we empirically apply the fixed length $\Delta t = 5$ minutes to satisfy the above requirement to the largest degree. Furthermore, to minimize contribution by noise, we filter out low values of $\dot{\Phi}$. Cross-correlation is performed in a given interval only when the maximum of $\dot{\Phi}_p(t_i, t_i + \Delta t)$ and $\dot{\Phi}_n(t_i, t_i + \Delta t)$ during this interval is above a certain cutoff value, which is empirically chosen to be 5×10^{17} Mx s^{-1}, or about 10% of the maximum reconnection rate in individual cells. We perform cross-correlation within the 5 minute running interval to obtain time profiles of correlation coefficients $\rho_{pn}(\tau_i)$, where $\tau_i = t_i + \Delta t/2$, for all combinations of the positive and negative cells involved in magnetic reconnection, and pick out pairs of cells that exhibit significant correlation $\rho_{pn}(\tau_i) \geqslant 0.5$ in three consecutive intervals. A good correlation within three consecutive intervals is required in order to minimize contribution by fluctuations on short timescales, which are likely caused by noise. Note that the requirement for balance between positive and negative reconnection fluxes is not implemented in the correlation analysis. Instead, we compute the ratio (R) of the total positive flux to the total negative flux integrated in cells that are picked out from the correlation analysis to monitor how well the automated sequence analysis observes the flux balance rule.

Figure 6 shows time profiles of correlation coefficients $\rho_{pn}(\tau)$ between positive (P) and negative (N) magnetic cells superimposed with the net reconnection rate (the mean of reconnection rates from the positive and negative polarities) as a reference. Only P–N pairs with significant reconnection flux and correlation larger than 0.5 are illustrated in this figure. It is clearly shown that, at different stages, different pairs of magnetic cells are "reconnecting." The correlation coefficient profiles $\rho_{pn}(\tau)$ nearly evolve along with the stage-wise reconnection rate. These results are also summarized in Figure 7 (top panel), showing the time sequence of pairs of reconnecting magnetic cells that are picked out by the analysis. The symbols in the figure indicate the positive and negative cells with correlated reconnection rates during the 5 minute interval centered at a given time bin $\tau_i = t_i + \Delta t/2$. Note that in this figure only pairs of cells with significant correlation (above 0.5) in $\geqslant 3$ consecutive time bins are selected.

From these figures, we group the correlated pairs in a time sequence of five episodes: 44–49, 49–54, 54–62, 62–67, and 67–75 minutes after 15:00 UT. The sequence of reconnection across these episodes is read off the plots as the following: P7/N1, P5/N1, P3/N2 $\longrightarrow$ P5/N3, P6/N3-1-2, P9/N1 $\longrightarrow$ P3-5/N1-2, P9/N1, P1/N2-3-1, P6/N1-2-3 $\longrightarrow$ P15/N1 $\longrightarrow$ P1/N1-3, P4/N3, P15/N1 (also see Table 2). Note that some correlated pairs span two episodes. Within each episode, the order of pairs generally indicates sub-sequences, though we do not further investigate them given the time interval (5 minute or 10 time bins) we require for the correlation analysis. Magnetic reconnection starts at sites next to the PIL in the major magnetic cells and spreads nearly along the PIL. The elongation pattern is

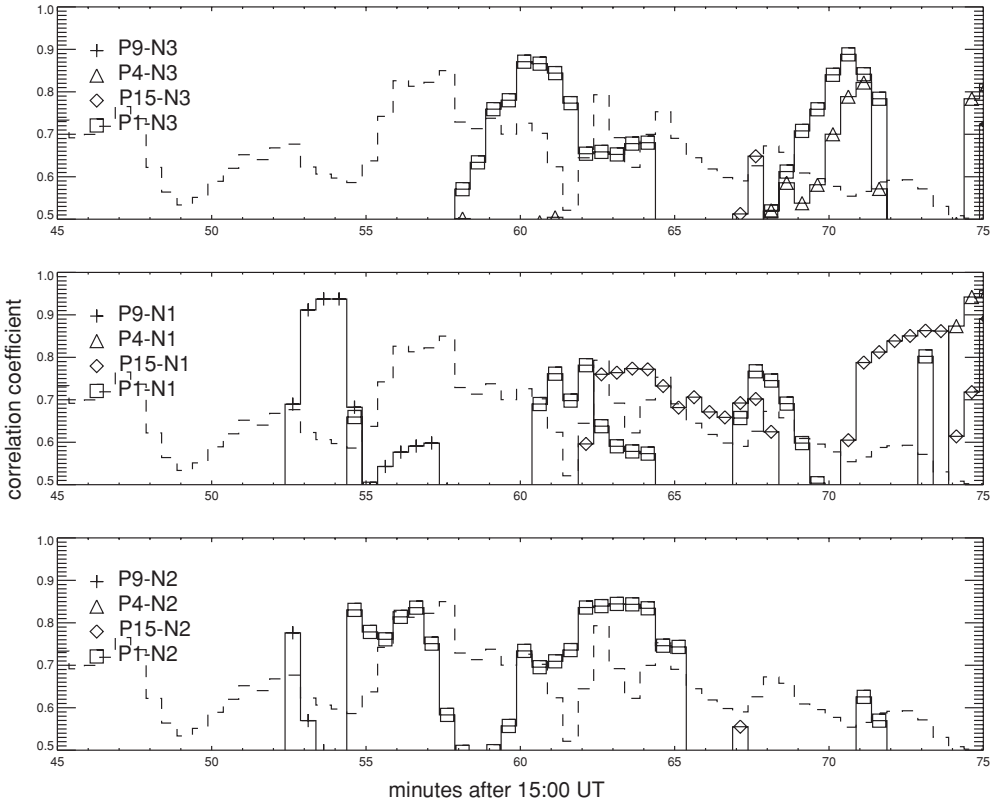

Figure 6. (Continued)

most evident from 49 to 54 minutes. Seen from Figure 2, in the negative polarities, sequential reconnection occurs along N3, N1, and N2, and in the positive polarities, the spreading along the PIL takes place in P7, P3, and P5, and then reconnection involves cells P9 and P6 in the western portion of the active region. Magnetic reconnection during the first stage plays the role of forming the skeleton of two ribbons along the PIL in nearly a sequential manner. Into the second stage, a greater number of magnetic cells are participating in reconnection. In the positive polarity, reconnection involving P3 and P5 proceeds into P4 and P15, both further away from the PIL, and in the negative polarity, reconnection proceeds within N3 and N1, in directions nearly perpendicular to the local PIL. Ultimately, reconnection sequence ends at P4, P15, N1, and N3 in the core region, as well as P1 in the western portion.

The *reconnection sequence analysis* is able to produce a major reconnection sequence characterizing how individual magnetic cells participate in reconnection. This result indicates that magnetic reconnection in the corona, on the one hand, does not exhibit a smooth and continuous evolution, and on the other hand, is not entirely chaotic. That magnetic reconnection proceeds sequentially, but not smoothly, between individual magnetic cells is most pronounced in Figure 7 (top panel), which reveals different pairs of magnetic cells picked out by the correlation analysis at different episodes (or peaks). The distinctive patterns are evident not only between the two stages, the parallel elongation and the perpendicular expansion, but also during different episodes on shorter timescales. For example, during expansions from P5 to P15, the rise of the reconnection rate around 64 min is coincident with reconnection penetrating into the strong field region of P15. Similarly, reconnection peaks around 67 minutes are coincident with expansion from P3 to P4 and from N2 into N8. Note that most peaks in reconnection rates are registered in a few magnetic cells in both polarities, therefore, these peaks are a reflection of the coronal process rather than artifacts of analyzing highly structured photospheric magnetograms.

We note that the *reconnection sequence analysis* is a first-order approach, as we spatially resolve the reconnection rate on scales of individual flux cells other than at pixel level and temporally resolve reconnection on 1 minute timescale, which is much longer than the observing cadence of 2 s. This is sensible, because below these macroscopic scales, the nature of reconnection is perhaps more sporadic than ordered. It is noted that even at the present temporal-spatial scales, all cells in reconnection cannot be picked up by the correlation analysis. For example, early in the second episode (49–54 minutes), judged from $\dot{\Phi}$ time profiles, P9 and N3 are likely correlated hence reconnecting ahead of P6/N3, but the P9/N3 pair is not selected by the automatic analysis procedure because $\dot{\Phi}$ in P9 is lower than the low cutoff value of 5×10^{17} Mx s^{-1}. Because of very low $\dot{\Phi}$, N8 and N12 are also discarded in the correlation analysis, though they participate in reconnection after 60 minutes. To have a sense of how well the correlation analysis works, we sum up reconnection flux in all the correlated pairs picked up by the automated analysis and derive the fraction of correlated flux to the total reconnection flux at given time bins as shown in Figure 7 (bottom panel) as well as in Table 1.[4] It is found that on average over three quarters of the total reconnection flux is picked by the correlation analysis, and the remainder is

[4] Note that the total correlated flux in each episode is computed differently in Table 1 and in Figure 7 (bottom panel): in the table, only reconnection flux in each episode is computed, and in the figure, at each point, the values of reconnected flux and flux ratio are computed from integral over the 5 minute box centered at the given time bin.

Table 1
Reconnection Sequence

Episodes (Minutes After 15:00 UT)	44–49	49–54	54–62	62–67	67–75
Correlated Pairs	P7/N1 P5/N1 P3/N2	P5/N1[a] P3/N2[a] P5/N3 P6/N3-1-2 P9/N1	P3/N1-2 P5/N1-2 P9/N1 P1/N2-3-1 P6/N1-2-3	P6/N3-2[a] P1/N3-1-2[a] P15/N1	P1/N1-3 P4/N3 P15/N1
Total Reconnection Flux[b]	1.21/0.69	0.74/0.75	2.04/2.06	1.09/1.03	0.80/0.45
Flux Ratio (P/N)	1.77	0.99	0.99	1.07	1.78
Total Correlated Flux[b,c]	1.21/0.65	0.57/0.69	1.92/2.00	0.75/0.97	0.75/0.31
Flux Ratio (P/N)[c]	1.87	0.83	0.96	0.77	2.43

Notes.
[a] This correlated pair is apparently continued from the previous episode.
[b] The reconnection flux is in units of 10^{21} Mx, and the numbers before and after the "/" indicate fluxes in the positive and negative polarities, respectively.
[c] The reconnection flux is calculated for each episode without taking into account the 5 minute box applied in the correlation analysis, different from Figure 7 (bottom panel).

Table 2
Reconnection Flux[a]

Positive Cells	P1	P3	P4	P5	P6	P7	P9	P15
Total Magnetic Flux (10^{21} Mx)	6.8	1.7	2.2	1.1	1.2	0.3	0.5	0.8
Obs. Reconnection Flux (10^{21} Mx)	1.2	1.5	0.3	1.0	0.5	0.0	0.2	0.3
Model Reconnection Flux[b] (10^{21} Mx)	0.61	0.89	0.47	0.88	...	...	...	0.24
Total Reconnection Flux (Fraction)	18%	89%	13%	87%	38%	6%	33%	39%
Reconnection Flux in First Stage	0%	47%	0%	47%	10%	6%	2%	3%
Reconnection Flux in Second Stage	18%	42%	13%	40%	28%	0%	31%	36%
Negative Cells	N1	N2	N3	N7	N8	N12		
Total Magnetic Flux (10^{21} Mx)	5.3	3.1	2.5	1.8	0.9	0.5		
Obs. Reconnection Flux (10^{21} Mx)	1.5	1.4	1.5	0.0	0.1	0.0		
Model Reconnection Flux[b] (10^{21} Mx)	1.43	0.50	1.19	0.34	...	...		
Total Reconnection Flux (Fraction)	29%	46%	61%	2%	13%	7%		
Reconnection Flux in First Stage	9%	8%	16%	1%	0%	0%		
Reconnection Flux in Second Stage	20%	38%	45%	1%	13%	7%		

Notes.
[a] Unless indicated, the reconnection fluxes listed in the table refers to observationally measured fluxes.
[b] The model predicted reconnection flux in a given cell is computed from Table 1 in Longcope et al. (2007) by averaging all the fluxes donated ($\Delta\Psi_{\downarrow}$ in their paper) and received ($\Delta\Psi_{\uparrow}$) by this cell.

not apparently correlated. In the same plot, we also show the ratio of positive to negative flux from correlated cells. The flux ratio usually deviates from unity but the median value comes close to unity and within the range of uncertainties (see Qiu et al. 2007). When broken down into the five episodes, as shown in Table 1, it is seen that there is relatively larger flux imbalance in the first and last episodes, which may be caused by the low reconnection rate leading to inaccurate estimates. The above analysis provides a qualitative measure of how well the sequence analysis works. Both physical and unphysical reasons contribute to the flux imbalance. Unphysical reasons include uncertainties in both the reconnection flux measurements from flare signatures and the partitioning of the magnetogram, and the limitation of the present method of correlation analysis. Physically, although our analysis with the presently designated temporal and spatial scales captures the major reconnection sequence faithfully, on fine scales, magnetic reconnection may proceed in a more complex manner than following a single major sequence.

Magnetic reconnection is thought to relax the pre-reconnection magnetic field to a low-energy configuration by allowing flux exchanges between magnetic domains. The amounts of flux exchange, or reconnection fluxes, between magnetic cells are measured from observations. Observations reveal that each of most magnetic cells does not participate in magnetic reconnection by its entirety. Table 2 lists the amount of reconnection flux as a fraction of the total flux in each magnetic cell. In the major cells P3, P5, N3, and N2, reconnection flux makes close to or more than half of the total flux, while in other cells, reconnection flux is less than half of the total flux. Also given in the table is the amount of reconnection flux during two stages divided at 54 minutes. For comparison, we also compute the model predicted reconnection flux by Longcope et al. (2007). The predicted reconnection flux in each cell is the mean of the total received flux $\Delta\psi_{\uparrow}$ and total donated flux $\Delta\psi_{\downarrow}$ (in absolute values) in this cell. The observational measurements of reconnection flux presented here are systematically larger than the numbers from the model prediction, because in this paper we use the photospheric magnetogram without extrapolation to higher altitudes, and a lower threshold for the flare radiation and no frame integration to emphasize weak features. These different steps can raise the measured reconnection flux by about

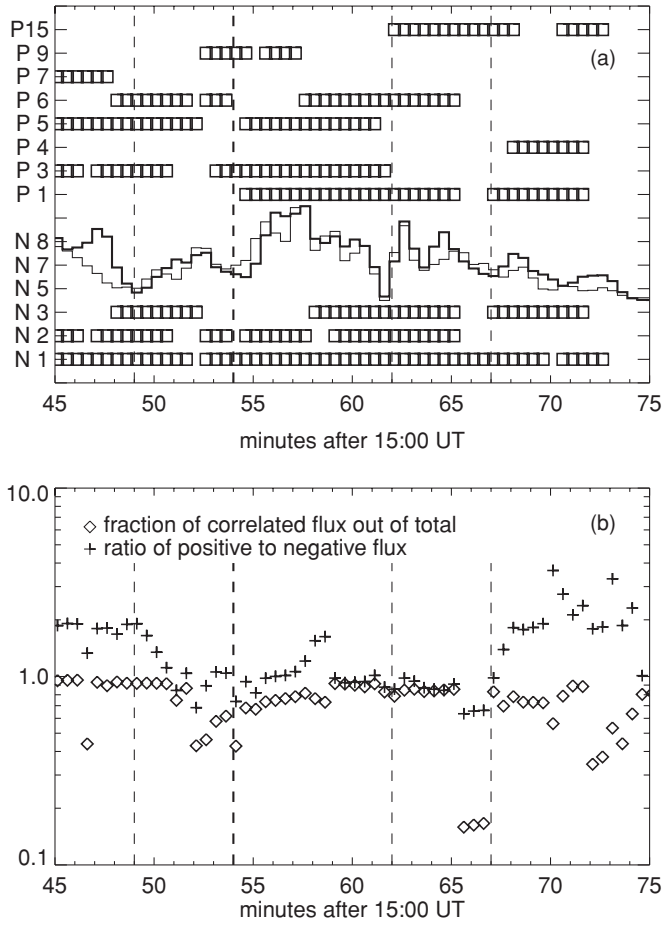

Figure 7. Summary plot of reconnection sequence. (*a*): the time evolution of connectivity. Symbols indicate magnetic cells whose reconnection rates are correlated with cells in opposite polarities within a 5 minute box centered at the times. The curves indicate the net reconnection rate derived in the positive (thick solid line) and negative (thin solid line) polarities, respectively, normalized to arbitrary units. (*b*): net reconnection flux summed over all the correlated cells as a fraction of the total reconnection flux (diamond symbols), and the ratio of positive to negative flux in reconnecting cells (plus symbols). In both panels, solid bars indicate five episodes of reconnection, and the thick solid bar at 54 minutes indicates the division of two major reconnection stages.

20%–30%, but do not affect the evolution pattern of reconnection flux and reconnection rate. Minor details may change when different sets of parameters are applied in the correlation analysis. However, our experiments show that these variations would not significantly modify the major reconnection sequence shown in the foregoing text. Such analysis, though with ample room for improvement, makes it possible to start comparing and bridging observations and models in order to uncover the true three-dimensional topology of magnetic reconnection. A brief discussion of the model–observation comparison will be given in Section 5.

5. DISCUSSIONS

5.1. Three-Dimensional Evolution of Magnetic Reconnection

Results from the above two sections may be combined to arrive at a picture of the three-dimensional evolution of connectivity between magnetic cells. Figure 8 shows the sketch of the reconnection sequence at each given episode as determined from the reconnection sequence analysis (see Table 1). In the figure, the pairs of major reconnecting cells determined from correlation analysis are connected by dashed lines, and the arrow on each cell indicates the direction of the spread within the cell. As the reconnection sequence alone cannot distinguish the pre-reconnection and post-reconnection connectivities, we assume that the correlation pattern, which is obtained by employing radiation signatures, indicates the post-reconnection connectivity. In other words, the correlated pairs of cells are considered to be feet of postflare loops.

In this context, it is seen that in the precursor episode arcades of postflare loops are formed in a sequence. Formation of loops connecting P5 and N1 spreads to the west, and formation of loops connecting P3 and N2 spreads to the east, suggestive of "unzipping" of magnetic reconnection along the axis of low-lying arcade. Note that these low-lying loops inferred from the correlation analysis would be sheared with respect to the PIL. The pattern of connectivity changes sharply from 49 to 54 minutes, when we see a rapid westward elongation along P5–P9–P6 in the positive polarity, and meanwhile an eastward elongation from N3 to N1 and then N2, resulting in the connectivity of P5/N3, P9/N3-1, and P6/N3-1-2. Note that this is also the stage with the most rapid elongation primarily along the PIL, with the apparent speed at times larger than 100 km s^{-1}, comparable to the local Alfvén speed. If the inferred connectivity refers to the post-reconnection connectivity, this stage would characterize the formation of long loops connecting P9/N3-1[5] and P6/N3-1-2, which are nearly parallel to the PIL, together with shorter loops connecting P5 and N3, which are more perpendicular to the PIL. After 54 minutes, the connectivity pattern would indicate the formation of loops connecting the outer edges of P3 (extended to P4), P5 (extended to P15) and N1–N3, as well as P1 and N-cells, which are more perpendicular to the PIL. In summary, the reconnection sequence suggests the following three-dimensional evolution of magnetic reconnection: the formation of short sheared low-lying loops, the formation of long loops nearly parallel to the PIL, and the formation of overlying loops more perpendicular to the PIL.

Change of connectivities between source magnetic cells by magnetic reconnection carries along helicity transfer between different magnetic structures. One plausible consequence of the helicity transfer is the formation of a flux rope by converting the mutual helicity of sheared pre-flare loops to the self-helicity (twist) of the rope (van Ballegooijen & Martens 1989; Longcope et al. 2007). The reconnection sequence (particularly during the elongation) from above analysis implies such a likely scenario. Hypothetically, during the stage of rapid directional elongation, the formation of long loops would make the axis of the posterior flux rope, and reconnection in the ensuing expansion stage adds twists to the flux rope. The sequence analysis suggests that P1 and N1 or N3 might become the feet of the rope. The total reconnected flux in P1 and N3 would set an upper limit of the rope flux, which is 1.2 to 1.5 $\times$ 10^{21} Mx. The poloidal flux of the rope (or the amount of twist), if in a simplified manner conjectured by Moore et al. (2001), Longcope et al. (2007, Figure 1), Qiu et al. (2007), and Moore et al. (2007), would be very close to the arcade flux threading from P3/4-P5/15 to N1-2-3 formed by reconnection during the second (perpendicular expansion) stage, amounting to (3–4) $\times 10^{21}$ Mx. Therefore, the hypothetical flux rope has at least two to three turns per unit length on average. The sense of the flux rope is

[5] In the following text and Figure 8, we include the pair P9/N3 in the second episode from visual inspection of their $\dot{\Phi}(t)$ profiles, though it is not picked out by the automated correlation analysis.

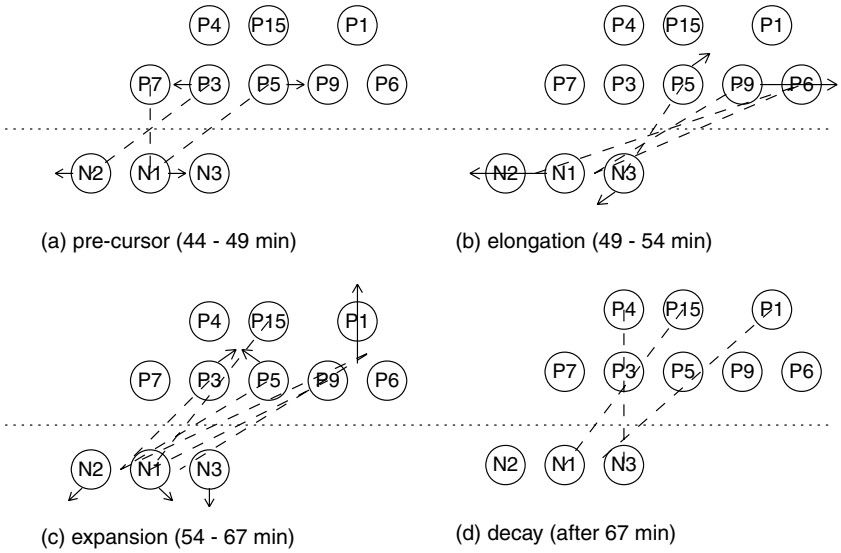

Figure 8. Sketch of connectivities between magnetic cells and evolution of cell brightening with respect to PIL during the flare. In each panel, circles give the relative positions of major magnetic cells that participate in reconnection and the dotted line marks the PIL. Dashed lines connect positive and negative cells that are reconnecting at a given episode as determined from the sequence analysis. Arrows give the direction of the spread of brightening in the cell with respect to the PIL.

left handed, same as the interplanetary flux rope manifested as a Magnetic Cloud (Longcope et al. 2007). Rigorous computation of the helicity transfer and amount of twist in a full three-dimensional approach, however, has to occur only when the prior connectivity is known or modeled. The reconnection sequence analysis alone cannot answer this question. A preconnection topological structure of the corona has to be given, such as in Longcope et al. (2007).

With the notion above, we briefly discuss how the observationally inferred reconnection sequence compares with predictions from the topological model (Longcope et al. 2007). Both agreement and discrepancies are found between the two independently determined sequences. The topology model predicts the following sequence in the positive polarity P5$\longrightarrow$P15$\longrightarrow$P13$\longrightarrow$P8$\longrightarrow$P4, and in the negative polarity, the sequence follows along N3$\longrightarrow$N1$\longrightarrow$N2. In comparison with observational measurements, the topological model captures the general direction along which flare ribbons form, particularly in the negative polarity, though it does not distinguish the two-stage reconnection within individual cells as revealed in observations. Effectively, the topological model combines the two stages, the parallel and perpendicular expansions, observed in the flare evolution into one. It remains to be investigated what is the physical implication of the observed two-stage evolution to topologic models of reconnection. Quantitatively, the model is able to include most magnetic cells that are involved in reconnection as revealed by flare observations, and the computed reconnection flux in each cell is comparable with observational measurements for the majority of reconnecting cells. As illustrated in Table 2, the model captures five cells (out of the observed eight) in the positive polarity, and four cells (out of the observed six) in the negative polarity. Given that the observational measurements in this paper are the upper limits of the range of values, we may consider that the reconnection fluxes from model computation and from observational measurements are consistent and closely comparable in three major positive cells (P3, P5, P15) and two major negative cells (N1 and N3), with minor discrepancies well within the range of uncertainties in measuring the reconnection flux from observations as well as determining connectivities in the model. Other discrepancies include the following: in the positive polarity, the model does not consider P6 and P9, and overestimates the flux in P4, P2, and P13 in comparison with observations; in the negative polarity, the model underestimates the flux in N2 and overestimates the flux in N7 and N10. However, it is noted that the contribution of reconnection flux by these significantly mismatched cells is small, which makes up to 30% of the total reconnection flux. This though very crude first-order comparison shows a good degree of agreement between entirely independent determinations of reconnection fluxes in individual cells given uncertainties in both methods, which may suggest that the model reasonably represents the observed evolution of reconnection, and, therefore, the change to the helicity and energy estimates by adjusting the model to better reproduce observations may be expected to be minor. In an ensuing study, we will conduct detailed comparisons between the model and observation and discuss the implication of the comparison.

5.2. Energy Release

Reconnection releases energy by converting free magnetic energy into heating plasmas and accelerating charged particles as well as bulk plasmas. The rate of energy release is governed by macroscopic corona field configuration and microscopic physics of magnetic reconnection. Among important physical quantities characterizing magnetic reconnection, the macroscopic rate of magnetic reconnection may be inferred by employing the flux conservation principle as performed in this paper. The macroscopic reconnection rate is equivalent to the induced electric field (E_c) integrated along the length of the current sheet, and the work done by this field on the current is equivalent to the amount of energy release by magnetic reconnection in the corona. Our knowledge of this other key parameter, current (I_c) or the effective resistivity (η_c), has been largely a matter of guess.

To make a step closer to understanding energy release, we probe the relation of the energy release rate to the reconnection rate so as to shed light on this critical but hardly measurable parameter. Existing observing facilities cannot yield a direct measurement of the total energy released by reconnection during a flare, and in this discussion, we only employ an estimate of thermal energy as an approximation to flare energy release.

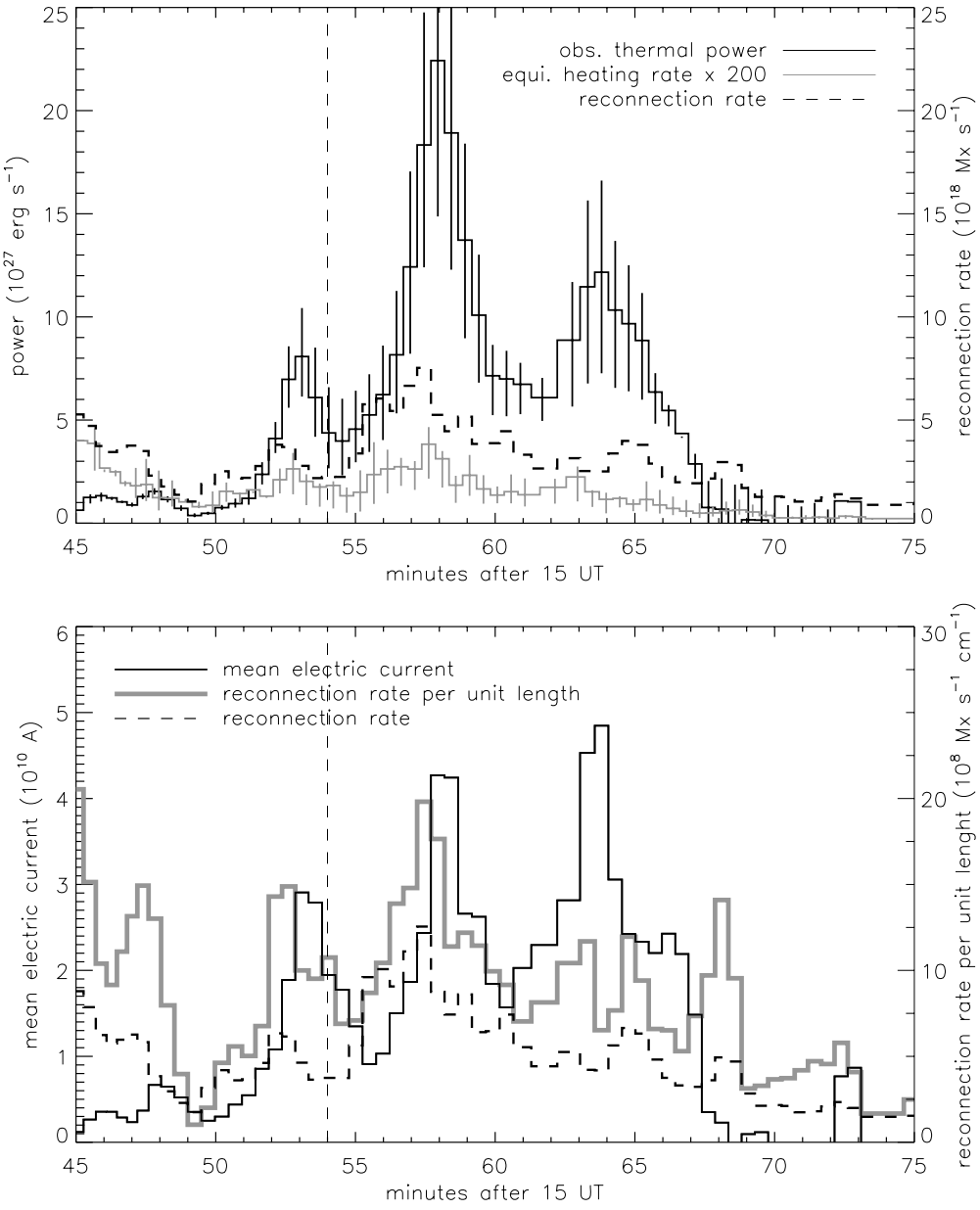

Figure 9. Estimates of reconnection energy release and reconnection electric current. Top: the observed thermal energy release rate estimated from *GOES* diagnostics and the morphological evolution of the flare (dark solid line) and the estimated equilibrium heating rate from the scaling law (gray solid line). Vertical bars indicate the range of the estimates. The dashed curve shows the total reconnection rate. Bottom: mean electric current (dark solid line), reconnection rate per unit length (gray solid line), and total reconnection rate normalized to arbitrary units (dashed line). In both panels, the vertical dashed bar at 54 minutes indicates the division between two major stages of the flare.

To derive thermal energy, we combine diagnostics of thermal plasmas emitting X-ray continuum to be observed by *GOES* at two broadbands and information of the geometry of the flare inferred from our analysis in Section 3. For the first-order approximation, we only look at the global evolution (Figure 4) and assume a 2.5D geometry of the flaring arcade. For the estimate, we assume that at each time interval the newly brightened patches in the opposite polarities outline the feet of newly formed coronal loops in an arcade, each loop in an arcade is semicircular with a constant cross-sectional area from the feet to the loop apex, and the filling factor is unity in the flaring corona. Therefore, at each time frame, we find the mean length l of newly formed loops from the instantaneous mean distance of their feet to the PIL by $l = \pi d_{\perp}$, and the cross-sectional area δA of the loops as newly brightened areas at the feet, thus determine the volume of newly brightened loops as $\delta V = l\delta A$. The instantaneous volume of all loops V at a given time is the sum of δV over time. With the mean temperature T and emission measure $G = \int n^2 dV$ determined from *GOES* diagnostics, we may estimate the thermal energy in units of erg $U(t) = 3nkTV$, and the radiative loss in units of erg s^{-1} $L_{\rm rad} \approx 6 \times 10^{-22}(T/10^5)^{-1/2}G$ (Veronig et al. 2005). Considering only these terms, the instantaneous energy release rate by the explosive energy release during the flare is given as $P_{\rm exp} = \partial U/\partial t + L_{\rm rad}$. Contribution of $L_{\rm rad}$ is an order of magnitude smaller than $\partial U/\partial t$, and becomes non-negligible only during the last few minutes of the flare.

Figure 9 shows the thermal power $P_{\rm exp}$ evolving with time. The vertical bars in the plot indicate the range of values resulting from computations using quantities determined for P-ribbon

and N-ribbon separately, and using a variety of temporal and spatial smoothing parameters. It is seen that $P_{\rm exp}$ is correlated with the reconnection rate with a 1–2 minute lag, as also seen, not surprisingly, in the direct time derivative of the *GOES* soft X-ray light curve (Figure 3). The estimated $P_{\rm exp}$ including only those thermal energy terms is about 2×10^{28} erg s^{-1} at the peak, and the total thermal energy integrated over the 20 minute duration of the flare amounts to 8×10^{30} erg. The ratio of the thermal energy release rate to the reconnection rate yields the mean instantaneous current I_c in the reconnection region, as shown in Figure 9 (bottom panel). It peaks at 5×10^{10} A, and fluctuates during the flare. Note that despite an appreciable reconnection rate before 49 minutes the energy release rate is very low. This may suggest that the effective current is very small during the precursor stage when ribbons are impulsively "filling up," or it may be caused by a delay of plasma heating and radiation at *GOES* temperature. For this flare, hard X-ray observations by *RHESSI* missed the impulsive phase, so we cannot verify whether significant instantaneous nonthermal energy release takes place at the precursor. The mean effective resistivity along the length of the current sheet is estimated to be $\eta_c = \dot{\Phi}^2 / P_{\rm exp} l_{||} \approx 10^{-7}\ \Omega\ {\rm m}^{-1}$, where $\dot{\Phi}$ is the reconnection rate.

To compare the explosive energy release via magnetic reconnection during flares with other steady-state situations, we also estimate the heating rate of coronal loops in hydrostatic equilibrium, using the geometric quantities inferred in Section 3 and the scaling law given by Schrijver et al. (2004): $P_{\rm equ} = \partial E / \partial t = 1.4 \times 10^{14} B / l_l A$. The scaling law is derived from nonflaring long-lived coronal loops in active regions. In this relation, B is the magnetic field strength at the (chromosphere) feet of the loops, which is measured, in this paper, as the mean magnetic field encompassed by newly brightened ribbons. The time profile of $P_{\rm equ}$ is plotted in Figure 9. It is no surprise that $P_{\rm equ}$ is smaller than the observed explosive energy release rate $P_{\rm exp}$ by nearly 3 orders of magnitude, as the scaling law describes the corona heated in a steady-state process (Schrijver et al. 2004). Comparison between $P_{\rm equ}$ and $P_{\rm exp}$ yields that the effective resistivity or current during the explosive energy release is raised by 3 orders of magnitudes.

Note that the above estimate of the energy release rate has to deal with some assumptions, that energy released in reconnection is primarily (or ultimately) converted into thermal energy in arcades of semicircular loops, and that the cooling timescales are significantly long so that all heated plasmas are seen by *GOES* throughout the flare and evolve isothermally. In reality, during the early impulsive phase, flare loops are likely sheared as suggested by the sequence analysis in the foregoing sections, thus the current may be greater in the early phase than shown in the figure with a semicircular assumption. The second assumption of infinitely long cooling time puts our energy estimate as an upper limit of the thermal energy of plasmas detected by *GOES*, because of the dependence $P_{\rm exp} \sim \sqrt{V}$, V being maximized by the infinite cooling time assumption. Furthermore, comparison of timings of the reconnection rate and the thermal energy release rate ($P_{\rm exp}$) is meaningful only when the effective timescale of plasma heating (so as to radiate at the *GOES* temperature) relative to the timescale of evolution of magnetic reconnection (a few minutes) is understood. The apparent lag of the energy release rate with respect to the reconnection rate may be interpreted as due to the interplay of both the reconnection rate and the reconnection current (or effective resistivity) when the timescale of plasma heating is much shorter than the evolution timescale of magnetic reconnection. Finally, the above discussion is confined to energy release by a nonideal resistive MHD process (reconnection), which is, presumably, ultimately converted to thermal energy.

In addition, Figure 9 (bottom panel) also shows the mean reconnection rate per unit length along the PIL to be of order $(0.5–2)\times 10^9$ Mx s^{-1} cm^{-1}, equivalent to a mean electric field of 5–20 V cm^{-1} in the two-dimensional regime. Readers are reminded that although the figure shows an apparent peak of the reconnection rate per unit length at the precursor, it cannot be readily interpreted as the instantaneous reconnection electric field. The apparent motion of the flare ribbons before 54 minutes is primarily parallel to the PIL, or along the assumed direction of the reconnection current sheet, thus the apparent speed is not equivalent to the reconnection inflow speed as in the two-dimensional assumption. In general, the reconnection electric field $E_c = V_l B_l$ has to be measured with caution. When the flare evolution cannot be depicted by a two-dimensional model, or the apparent spread cannot be convincingly decomposed into a component perpendicular to the direction of the reconnection electric current, determination of $V_l B_l$ is dubious if not meaningless.

6. CONCLUSIONS

We employ the *reconnection sequence analysis* to find the temporal and spatial evolution of magnetic reconnection. We partition the photospheric magnetic field into individual cells, derive time profiles of the reconnection rate in these cells, and obtain the sequence of magnetic reconnection between these cells from a correlation analysis. The method is applied to an X2.0 two-ribbon flare occurred on 2004 November 7, which exhibits several episodes of magnetic reconnection. It is seen that the method can pick up pairs of magnetic cells that are reconnecting during these episodes in a sequential manner. The analysis yields physical quantities directly comparable with topological models, thus is promising to provide observational constraints to justify subsequent calculation of helicity transfer and energy release from the model. A brief model–observation comparison for one event in the present study shows reasonable agreement between independently determined physical quantities, though some details differ and deserve further investigation.

The analysis also reveals two distinctive stages of magnetic reconnection, namely, parallel elongation and perpendicular expansion of flare ribbons with respect to the PIL. Elongation of flare ribbons along the PIL during the first stage proceeds at apparent maximum speeds comparable with the Alfvén speed in the active region chromosphere, which may reflect the propagation of perturbation in the corona along the reconnection current sheet. The apparent perpendicular expansion speed, reflecting the reconnection inflow in the corona, is a fraction (up to 10%) of the local Alfvén speed. These two stages are also marked in time profiles of the reconnection rate and energy release. Although the elongation, or "unzipping" of flare ribbons, has been reported in traditional flare observations (see Moore et al. 2001, for the most comprehensive discussion) as well as discovered lately in three-dimensional MHD simulations of corona reconnection (Linton 2008), it remains unclear what are the physical mechanisms governing the division of the two distinctive stages of reconnection.

As the last remark, we note that the *reconnection sequence analysis* method has a few advantages. First, we directly examine the temporal and spatial evolution of the reconnection rate in a quantitative manner, which is physically more meaningful

than radiation signatures alone. Second, the method avoids some difficulties in using the radiation signatures for quantitative analysis, such as flat-fielding, nonlinear exposure treatment, seeing effects in ground-based observations, and unknown intrinsic physics such as cooling profiles of flaring atmosphere. These effects would produce fluctuations and uncertainties in emission signatures thus pose difficulty in interpreting their time profiles and correlation patterns. The *reconnection sequence analysis* only takes the message of the differential brightening area regardless of the intensity variations in the flaring region, thus avoiding all the above difficulties. The problem would occur with spatial fluctuations in the magnetograms due to either physical (such as evolution of magnetic fields) and unphysical reasons. The method is useful to deal with timescales of order 30–60 s, which is a compromise between instrumental time resolution and physical and unphysical conditions that require a smoothing procedure before analyzing the time profiles. The result of our analysis on a flare event suggests that the analysis on such timescales as well as spatial scales prescribed by the present partitioning method yields physically meaningful measurements to provide observational constraints for models.

The author thanks Dana W. Longcope, Richard C. Canfield, and Ronald Moore for insightful discussions, and the referee for constructively critical comments leading to significant improvement of the manuscript. I acknowledge *TRACE* and *SOHO* missions for providing quality observations. This work is supported by NSF grants ATM-0603789, ATM-0748428, and NASA grant NNX08AE44G.

REFERENCES

Barnes, G., Longcope, D. W., & Leka, K. D. 2005, ApJ, 629, 561
Demoulin, P. 2006, AdSpR, 37, 1269
Demoulin, P., Henoux, J. C., & Mandrini, C. H. 1992, Sol. Phys., 139, 105
Demoulin, P., Henoux, J. C., & Mandrini, C. H. 1994, A&A, 285, 1023
Des Jardins, A. C. 2007, PhD thesis, Montana State Univ.
Fletcher, L., & Hudson, H. 2001, Sol. Phys., 204, 69
Fletcher, L., Pollock, J. A., & Potts, H. E. 2004, Sol. Phys., 222, 279
Forbes, T. G., & Priest, E. R. 1984, in Solar Terrestrial Physics: Present and Future, ed. D. M. Butler & K. Paradupoulous (NASA), 1
Grigis, P. C., & Benz, A. O. 2008, SPD/AGU, SP 44A-05, Fort Lauderdale, Florida
Handy, B. N., et al. 1999, Sol. Phys., 187, 229
Isobe, H., Takasaki, H., & Shibata, K. 2005, ApJ, 632, 1184
Isobe, H., Yokoyama, T., Shimojo, M., Morimoto, T., Kozu, H., Eto, S., Narugake, N., & Shibata, K. 2002, ApJ, 566, 528
Kawaguchi, I., Kurokawa, H., Funakoshi, Y., & Nakai, Y. 1982, Sol. Phys., 78, 101
Kitahara, T., & Kurokawa, H. 1990, Sol. Phys., 125, 321
Krucker, S., Fivian, M. D., & Lin, R. P. 2005, Adv. Space Res., 35, 1707
Linton, M. G. 2008, SPD/Karen Harvey Prize Lecture, SPD/AGU, SP 42A-01, Fort Lauderdale, Florida
Liu, C., Lee, J., Deng, N., Gary, D. E., & Wang, H. 2006, ApJ, 642, 1205
Longcope, D. W. 1996, Sol. Phys., 169, 91
Longcope, D. W., Barnes, G., & Beveridge, C. 2009, ApJ, in press
Longcope, D. W., & Beveridge, C. 2007, ApJ, 669, L621
Longcope, D. W., Beveridge, C., Qiu, J., Ravindra, B., Barnes, G., & Dasso, S. 2007, Sol. Phys., 244, 45
Moore, R. L., & La Bonte, B. J. 1980, Proc. Symp., Solar and Interplanetary Dynamics (Dordrecht: Reidel), 207
Moore, R. L., Sterling, A. C., Hudson, H. S., & Lemen, J. R. 2001, ApJ, 552, 833
Moore, R. L., Sterling, A. C., & Suess, S. T. 2007, ApJ, 668, 1221
Neupert, W. M. 1968, ApJ, 153, L59
Poletto, G., & Kopp, R. A. 1986, in The Lower Atmosphere of Solar Flares, ed. D. F. Neidig (Sunspot, NM: NSO/Sacramento Peak), 453
Priest, E., & Forbes, T. 2000, in Magnetic Reconnection (Cambridge: Cambridge Univ. Press)
Qiu, J., Hu, Q., Howard, T. A., & Yurchyshyn, V. B. 2007, ApJ, 659, 758
Qiu, J., Lee, J., Gary, D. E., & Wang, H. 2002, ApJ, 565, 1335
Qiu, J., Wang, H., Cheng, C. Z., & Gary, D. E. 2004, ApJ, 604, 900
Saba, J. L. R., Gaeng, T., & Tarbell, T. D. 2006, ApJ, 641, 1197
Sakao, T. 1994, PhD thesis, Tokyo Univ.
Scherrer, P. H., et al. 1995, Sol. Phys., 162, 129
Schrijver, C. J., Sandman, A. W., Aschwanden, M. J., & DeRosa, M. L. 2004, ApJ, 615, 512
Su, Y., Golub, L., & van Ballegooijen, A. A. 2007, ApJ, 655, 606
Svestka, Z., & Cliver, E. W. , et al. 1992, in Eruptive Solar Flares, ed. Z. Svestka (Berlin: Springer), 1
van Ballegooijen, A. A., & Martens, P. C. H. 1989, ApJ, 343, 971
Veronig, A. M., Brown, J. C., Dennis, B. R., & Schwartz, R. A. 2005, ApJ, 621, 482
Vorpahl, J. A. 1972, Sol. Phys., 26, 397